

Automated design of scaffold-free DNA wireframe nanostructures

Received: 19 September 2024

Accepted: 7 May 2025

Published online: 20 May 2025

 Check for updates

Wen Wang ^{1,2,3,4,5,10}, Abdulmelik Mohammed ^{6,10}, Rong Chen^{1,2},
Antti Elonen ⁷, Silian Chen ⁸, Mengfan Tian ^{3,4,5,9}, Junhao Yang¹,
Ye Xiang ⁸ , Pekka Orponen ⁷  & Bryan Wei ^{1,2} 

Computer-aided design has become common practice in DNA nanotechnology, and many programs are available that make the sophisticated design processes accessible to both the core research community and curious scientists in other fields. However, most of the design tools are committed to the scaffolded DNA origami method. Here we present an automated design pipeline for creating DNA wireframe nanostructures based on a scaffold-free molecular self-assembly approach. Unlike in the DNA origami method, scaffold-free designs are not built around a global backbone strand but are constituted entirely of short, locally intertwined oligonucleotides. This overcomes many limitations inherent in scaffolded nanostructure designs, most notably the size constraints imposed by the length of available scaffold strands, and the topological and algorithmic challenges of finding feasible scaffold-strand routings. In practice, this leads to simpler design flows and opens up new design possibilities. To demonstrate the flexibility and capability of our approach, we generate a variety of complex DNA wireframe designs automatically from 2D and 3D mesh models and successfully realise the respective molecular nanostructures experimentally.

Through a steady progress of about four decades in DNA nanotechnology, the simple rules of Watson-Crick base pairing have come to enable the design of synthetic constructs of extraordinary diversity, complexity and controllability¹. In the early stages of this development^{2–6}, nanostructures of limited complexity were designed by joining single-stranded DNA (ssDNA) oligonucleotides together in specific complementary arrangements, with manual or semi-manual sequence generation. However, for the design of complex DNA nanostructures in the mega- to giga-dalton range, hundreds or thousands of ssDNA segments are involved, and automated design tools become necessary.

Most current DNA nanostructure design tools adopt the scaffolded origami approach^{7–10}, in which a long ssDNA scaffold strand (typically the ca. 7200 nt long genome of the M13 bacteriophage) is guided to fold into a desired target shape by domain pairings induced by a complementary set of short staple strands. Notably, the popular design program *cadNano*¹¹, which supports a compact arrangement of helices to match a desired target pattern, has provided a DNA nanostructure design pipeline accessible to researchers from different backgrounds. More recently, techniques for designing DNA nanostructures based on sparse wireframe helix layouts have been introduced to the methods portfolio, providing a rich extension to the

¹School of Life Sciences, Tsinghua University, Beijing 100084, China. ²Center for Synthetic and Systems Biology, Tsinghua University, Beijing 100084, China. ³BGI Research, Beijing 102601, China. ⁴BGI Research, Shenzhen 518083, China. ⁵BGI Research, Changzhou 213299, China. ⁶Department of Biomedical Engineering, San José State University, San José, CA, USA. ⁷Department of Computer Science, Aalto University, Espoo, Finland. ⁸Beijing Advanced Innovation Center for Structural Biology, Beijing Frontier Research Center for Biological Structure, Center for Infectious Disease Research, Department of Basic Medical Sciences, School of Medicine, Tsinghua University, Beijing 100084, China. ⁹College of Life Sciences, University of Chinese Academy of Sciences, Beijing 100049, China. ¹⁰These authors contributed equally: Wen Wang, Abdulmelik Mohammed. ✉ e-mail: yxiang@tsinghua.edu.cn; pekka.orponen@aalto.fi; bw@tsinghua.edu.cn

design space. Similarly to what *caDNA* brought to the field, automated design tools for wireframe architectures such as *vHelix*¹² and the *DAEDALUS/Athena* toolkit^{13,14} have promoted the general adoption of these schemes.

As an alternative, the scaffold-free molecular self-assembly approach^{15,16} overcomes limitations intrinsic to scaffold-based methods and presents new opportunities in DNA self-assembly. In this approach, individual components to be self-assembled partake in only local interactions with designated neighbours, reminiscent of the composition mindset of LEGO™ bricks in the macroscopic world. Scalability of the approach has already been demonstrated in single-stranded tile/brick designs¹⁷, where some of the resulting structures were much larger than typical origami structures created using the M13 genome as scaffold. The scaffold-free approach also avoids several complexities and constraints inherent in global scaffold-strand routings, which both simplifies the design method and broadens the design space.

In this study, we present an automated design pipeline for creating scaffold-free, 2D and 3D braided DNA wireframe structures (BRAIDS). Our production scheme enables streamlined design and fabrication of large and complex scaffold-free wireframe structures with fine structural features, as we shall demonstrate with a number of 2D and 3D examples. To the best of our knowledge, most of the wireframe structures presented in this study are much larger than the scaffolded counterparts. Our mesh models contain almost exclusively triangular faces, because structural flexibility is a typical challenge for wireframe DNA nanostructures, and face triangulation is a common strategy to counteract this. Most of the resulting structures in this study demonstrate substantial structural rigidity without excessive deformation from the targeted designs.

Results

Design pipeline

Polygonal meshes are routinely used in 3D graphics as discrete representations of the surfaces of 3D objects. Briefly, a *polygonal mesh* is a collection of polygonal *faces* that have been glued together along their edges to span the surface of a target shape. The BRAIDS pipeline is formulated to broadly and generally cover polygonal meshes of arbitrary shapes whose surface is an *orientable 2-manifold with* (possibly empty) *boundary* (cf. Supplementary Note 1). This mesh family subsumes, in particular, the surfaces of all 3D polyhedra that enclose a single continuous volume, and 2D meshes with disjoint holes. The wireframe of a mesh is a graph that comprises the vertices and edges of the mesh, embedded in 2D or 3D space as delineated by the mesh model.

The BRAIDS design scheme starts by routing circular strands along the boundaries of the mesh faces and holes in their prescribed clockwise orientations (Fig. 1A, B). Since each edge is now traversed twice in opposite directions by the orientation of the adjacent faces and/or holes, the circular strands are oriented in antiparallel manner on each edge, as desired for the formation of DNA double helices. In general, the intertwining of strands in helices would lead to topological linking of circular strands, but in the BRAIDS pipeline this concern is

precluded by the strands being nicked in a staggered manner on each edge so that each pair of neighbouring edges is bridged by an untangled linear strand (Fig. 1C). The strand crossovers at each vertex create a connected junction, because the crossovers link pairwise neighbouring edges in a cyclic order around the vertex. Details of the design specifications can be found in Supplementary Note 2.

To evaluate the scalability and generality of the design procedure, we designed and synthesised a number of 2D and 3D wireframe nanostructures. The details of the design process and the experimental protocols are presented in the Methods section. Briefly, a desired 2D or 3D mesh was first generated and rendered into short ssDNA splints according to our strand routing and nicking scheme (Fig. 1D). With the strand arrangement determined, segmentation and pairing information were used to generate the respective sequences. Structure formation was optimised for annealing protocols, strand concentration and buffer condition, as confirmed by native agarose gel electrophoresis, atomic force microscopy (AFM) and cryogenic electron microscopy (cryo-EM) (Fig. 1E).

2D wireframes

As indicated in an earlier study¹⁸, the geometric constraint of full face triangulation serves as an effective approach to maintain a defined geometry. We first designed a collection of 2D wireframe nanostructures based on fully triangulated meshes and six-arm junction motifs. Although the length of the edges in the mesh model can be arbitrary, the rendered DNA duplex lengths were rounded to be multiples of full turns (10.5 base pairs) so that the 5′ and 3′ ends of each strand in a duplex domain are on the same side, as desired in the routing. The duplexes were segmented into complementary domains according to a standardised scheme (Supplementary Fig 1). After a systematic investigation of different spacer lengths on a 16 × 3 (columns × rows) rectangular array of triangular faces (Supplementary Fig 2), three consecutive unpaired T bases (3 T spacer) were added at each junction to relax tension at the junction crossovers.

The first important feature of our design architecture is scalability. We first designed and constructed three rectangular arrays of triangular faces, constituted of 11 × 6, 17 × 9, and 23 × 12 triangles, and comprising respectively 220, 494, and 874 strands, with a total of 7480, 16796, and 29716 nucleotides (Fig. 2A–C). Successful structure formation was confirmed by both native agarose gel electrophoresis (Supplementary Fig 3) and AFM imaging (Fig. 2A–C and Supplementary Figs 4–6), witnessing the scalability of our design framework.

To further demonstrate the generality of our approach, we next designed and constructed two complex irregular structures representing the Chinese characters Luck (Fig. 2D) and Double Happiness (Fig. 2E), containing 782 and 1212 strands (26588 and 41208 nt) respectively. Structure formation was evaluated by agarose gel electrophoresis (Supplementary Fig 3). Subsequent AFM imaging (Supplementary Figs 7 and 8) shows homogeneous ensembles of the targeted structures with fine features, such as the small windows in the Chinese characters, attesting to the robustness of our design approach.

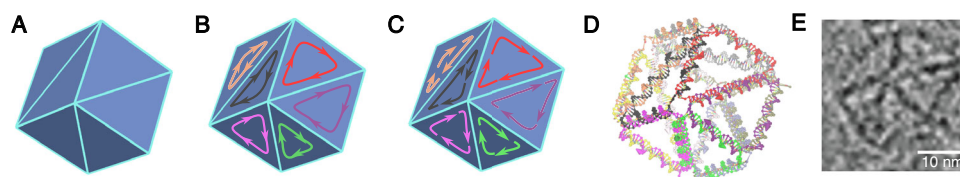


Fig. 1 | The BRAID pipeline for the design and assembly of a scaffold-free wireframe DNA nanostructure. **A** Triangulated cube mesh provided as input. (In general, the input can be any orientable polygonal mesh with or without boundary.) **B** Clockwise orientation of the faces of the mesh leads to a routing of circular strands that covers each edge twice. **C** Routing of a set of linear strands obtained by

a staggered nicking of the cyclic routings. **D** Nucleotide-level model of the DNA cube obtained by placing and nicking the helices according to the given routing scheme. **E** Sample cryo-electron micrograph of the eventual structure (scale bar: 10 nm).

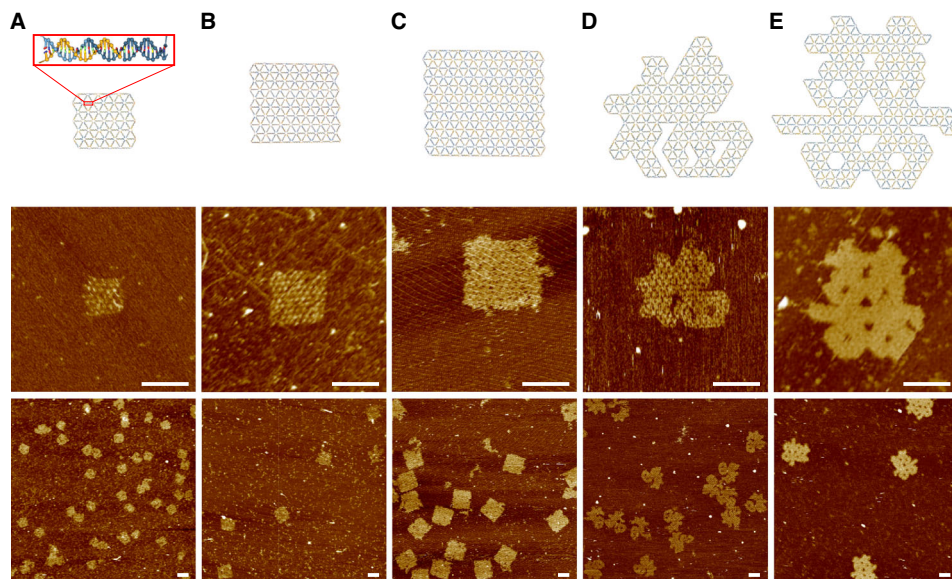


Fig. 2 | Design and assembly of 2D wireframe structures. **A** Rectangle shape comprising 11×6 triangular faces. **B** Rectangle shape of 17×9 triangular faces. **C** Rectangle shape of 23×12 triangular faces. **D** Chinese character Luck. **E** Chinese character Double Happiness. Top: nucleotide-level models; bottom: representative AFM images (scale bars for all images represent 100 nm, regardless of magnification). Zoom-in insert in **A**: rendering detail of an edge comprising a simple duplex.

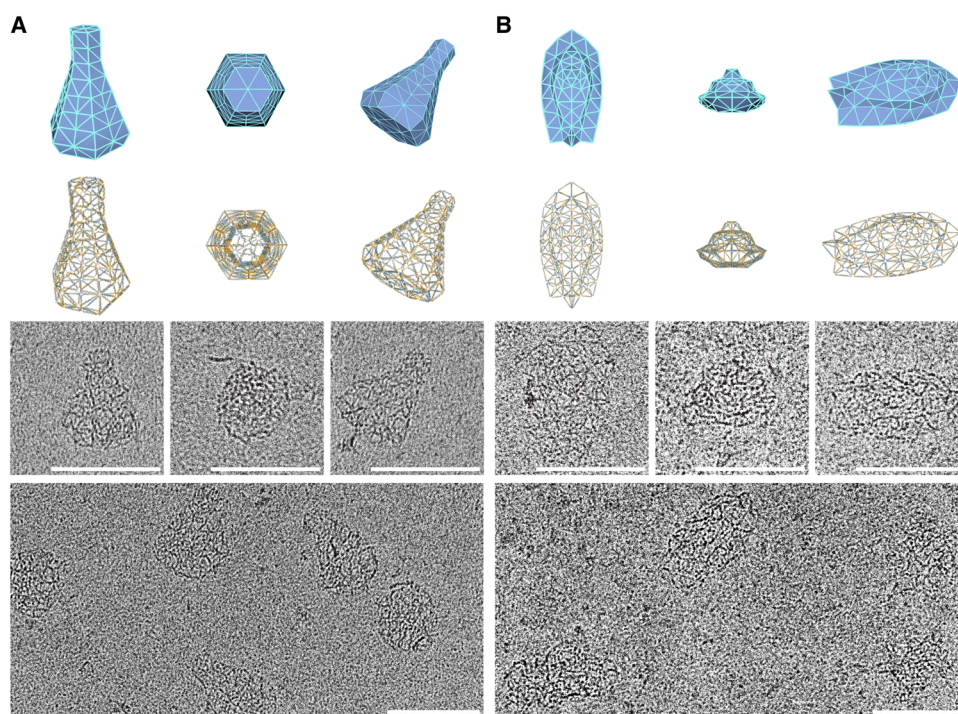


Fig. 3 | Design and assembly of 3D spherical wireframe structures. **A** Flask. **B** Submarine vessel Proteus. For each model, three representative views are presented. From top to bottom: triangulated mesh models; nucleotide-level models; representative cryo-EM images with selected views; large scale cryo-EM images. Scale bars for all images represent 100 nm, regardless of magnification.

3D wireframes

Also 3D wireframe structures based on meshes with polygonal faces can be created following the same principles. We explored the versatility of our approach by designing and assembling two classes of 3D constructs: wireframes based on spherical meshes (Fig. 3) and on non-spherical meshes (Fig. 4). By a *spherical mesh* we mean a surface mesh that is topologically equivalent to a sphere, i.e., can be continuously deformed into one. Non-spherical surface meshes on the other hand have one or more topological *handles*, or 3D holes.

Similarly as for the 2D designs with triangular faces, we subdivided the polygonal faces of 3D meshes into multiple triangles in order to rigidify the overall constructs. (In the mathematical sense, it is actually known that a convex polyhedral wireframe is structurally rigid if and only if its model mesh is fully triangulated¹⁹.) Unlike the 2D structures, which had a uniform edge length, in the 3D constructs the edge lengths vary according to the geometric requirements. The constructs were scaled to make the shortest edges at least 21 bp long to improve binding stability. The maximum vertex degree (number of junction

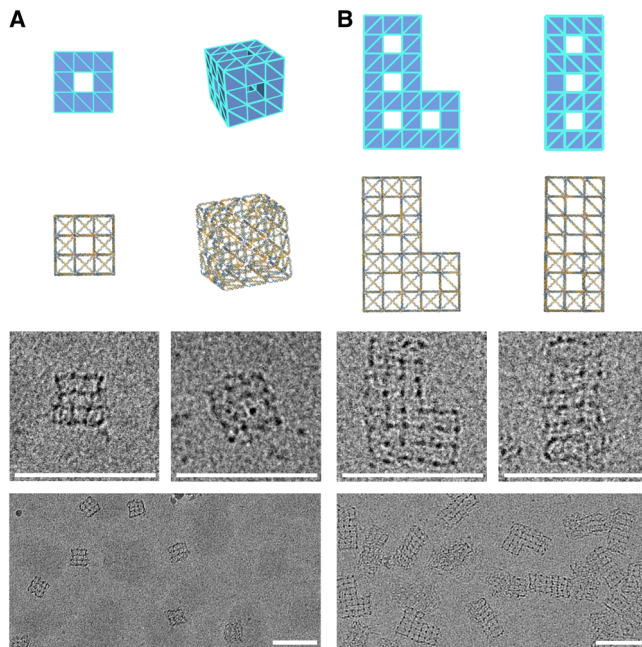


Fig. 4 | Design and assembly of 3D perforated multilayer wireframe structures. **A** Cube. **B** L-shape. For each model, two representative views are presented. From top to bottom: triangulated mesh models; nucleotide-level models; representative cryo-EM images with selected views; large scale cryo-EM images. Scale bars for all images represent 100 nm, regardless of magnification.

arms) was set to be eight and the sharpest acute angles were set to be 30 degrees.

Our first design was a Flask model with 722 strands (23862 nt, Fig. 3). The formation of the Flask structures was confirmed by native agarose gel electrophoresis (Supplementary Fig 9) and the morphologies were characterised by cryo-EM (Fig. 3A and Supplementary Fig 10), which shows desired structures in good agreement with the designs. We then continued with a more intricate model of the iconic submarine vessel Proteus from the 1966 film “Fantastic Voyage”, with 876 strands (30486 nt). Fine structural features, such as the sharp protrusions on the bow and stern of the submarine, can be observed in cryo-EM imaging (Fig. 3B and Supplementary Fig 11), suggesting our pipeline is a feasible method for the design and assembly of complex wireframe nanostructures.

Even though face triangulation was used to enhance the structural rigidity of these (nonconvex) designs, deformations were still present in the resulting constructs, notably in case of the Proteus particles. Compared to constructs with regular edge lengths, the irregular constructs with variable length edges had lower assembly yield, which in turn resulted in a limited number of particles in cryo-EM imaging. Moreover, the morphology of the particles was highly variable because of the structural deformations, so 3D reconstruction was remarkably challenging.

We were then prompted to explore regular wireframe designs based on non-spherical meshes, which make possible the creation of, e.g., some cubic lattices. In our earlier motif-based designs of multilayer nanocrystals²⁰, six-arm junction motifs branched out in a non-regular orientation, resulting in a lattice that was rhombohedral rather than cubic. With the present design approach, it is however possible to use triangulation to enforce square-shaped faces and thus create multilayer lattices of cubic arrangement. To demonstrate the feasibility of this design scheme, we first mapped out on a perforated cube surface a $3 \times 3 \times 3$ cubic lattice with 480 strands (14688 nt), in which the external faces were triangulated to maintain the overall cubic shape (Fig. 4A).

Formation of these multilayer cubes was evaluated by native agarose gel electrophoresis (Supplementary Fig 12), while morphologies were confirmed by cryo-EM (Fig. 4A and Supplementary Fig 13). The structural features were clearly demonstrated in the raw cryo-EM images, with uniformly distributed square 2D projection shapes, each of which is composed of nine small squares. When compared to earlier wireframe designs with non-cubic arrangement²⁰, the improvement of precise geometric control is substantial. To further illustrate the extent and scalability of this approach, we next designed a larger multilayer L-shaped $3 \times 5 \times 7$ nanocrystal with 1200 strands (37008 nt) in a similar fashion (Fig. 4B). Successful structural formation was verified by native agarose gel electrophoresis (Supplementary Fig 12), and cryo-EM imaging revealed designated 2D projections of different views (Fig. 4B and Supplementary Fig 14).

Unlike in the single-layer 3D constructs, the edge lengths and the strand segmentation were now more standardised (e.g., 31 bp for the square side edges and 42 bp for the diagonal edges). We believe this standard arrangement contributed to the improved assembly yield. Geometric constraints provided by triangulation and multilayer collective enforcement led to a much enhanced structural rigidity. With a combined enhancement of structural order and formation yield, cryo-EM imaging quality was substantially improved. With a greater design freedom and a higher material efficiency compared to a compact arrangement^{16,17}, this type of multilayer wireframe architecture provides greater scaffolding to host guest molecules of a wide size range, which can be beneficial in future application directions.

Discussion

In conclusion, we have developed a comprehensive, computer-supported design and production pipeline BRAIDS for wireframe DNA nanostructures using a scaffold-free approach. This approach is free of the size, sequence and topological constraints imposed by a globally routed scaffold strand, and the scalable freestyle design capacity also provides for finer structural details and more sophisticated meshes than previously accessible. The localised strand arrangement scheme supports the rendering of any oriented polygonal mesh, without concern for, e.g., knotted strand routings which are a challenge to the scaffolded origami approaches to wireframe DNA nanostructure design^{21–23}. Examples of complex meshes taking advantage of this characteristic are the cubical lattices presented in Fig. 4. Taking advantage of the new possibilities, we have demonstrated many 2D and 3D constructs with subtle structural features. Among the nanostructures realised, we successfully constructed sophisticated Chinese characters with small holes, intricate 3D models with fine features, and 3D cubic lattices.

Because the scaffold-free design approach bypasses the need for a global scaffold strand routing, it is also computationally both simpler and more general than the existing scaffold-routing based design techniques for wireframe structures (Table 1). In contrast to the Eulerian A-trail based method that underlies the *vHelix* tool¹², our design algorithm is guaranteed to converge in linear time in the size of the mesh (i.e., the number of mesh edges), whereas the A-trail algorithm is worst-case exponential. Even more importantly, the scaffold-free method subsumes all orientable polygonal meshes, of any genus and with or without boundary, while the A-trail method in its basic version requires the mesh to be sphere-equivalent. (However, the A-trail method has been extended to design and synthesise 2D meshes with boundary²⁴, and further algorithms have been developed for finding unknotted approximately Eulerian routings in higher-genus triangulated orientable meshes²²).

The spanning-tree based method used in the *DAEDALUS/Athena* family of tools^{13,14}, on the other hand, also has linear design algorithm runtime and encompasses all orientable polygonal meshes with (possibly empty) boundary. A characteristic of this method, however, is that it requires at least two parallel DNA duplexes for rendering each

wireframe edge, thus consuming in many cases twice the amount of scaffold strand used by the A-trail method for a comparable wireframe model. This makes the size- and complexity-scaling challenges for this method even greater than those for the A-trail method. (Clearly multiple-duplex edges can also be advantageous for increasing the rigidity of the synthesised nanostructures, and using the *Athena* toolkit¹⁴ even wireframes with six-duplex edges can be created).

Compared to our earlier motif-based design method²⁰, the top-down design approach presented here provides improved generality, flexibility and simplicity of use. In addition to the general increase in power and convenience delivered by an automated design pipeline, a structural design improvement is the triangulation of the mesh models, which constrains the angles between helices at mesh junctions and noticeably enhances the control of the eventual nanostructure shape as compared to the non-triangulated models in our earlier method.

Theoretically, there is no intrinsic size limit for DNA nanostructures designed using the scaffold-free approach, and in this work we have created a number of structures that are much larger than typical DNA origami constructs using the M13 genome as scaffold. However, assembly becomes more challenging for designs of increasing complexity. For example, for large or irregular structures we had to use much slower annealing protocols in the self-assembly process than for small and regular ones (Supplementary Fig 15). Similarly as has been observed in earlier self-assembly schemes for large structures with single-stranded DNA tiles or bricks^{15–17}, strands and segments with standardised settings resulted in the best outcomes for large constructs.

This design principle is however not applicable in the case of complex designs with irregular polygonal faces, such as our Proteus structures, as these inevitably involve non-uniform edge lengths. In such cases, it is possible for instance that the rendering of the mesh model edges as different non-integral multiples of DNA full turns results in unfavourable phase differences between consecutive helices, and these are not fully resolved by the spacer segments. Another possibility is that the stochastic bending of some longer edges in the structure propagates to create global deformations. When the thermodynamics and kinetics of such complex DNA self-assembly systems are better understood and modelled, one can envisage an optimised annealing protocol guided by theoretical principles rather than empirical engineering that will fully realise the scalability potential of the scaffold-free approach.

Also internal characteristics of the DNA nanostructures may play an important role. Global structural design (e.g., standard duplex length and segmentation), local structure features (e.g., crossover and nicking patterns), as well as details of the strand sequences all affect assembly efficiency and quality. Machine learning techniques could also be used for structure and sequence optimisation, taking advantage of the considerable datasets accumulated in the field²⁵. It is, therefore, desirable to understand the major factors that affect assembly yield when aiming for even higher levels of assembly complexity. By means of the implementations in this study and related ones^{20,26}, we have already achieved improved assembly yields by

structure/sequence optimisation (e.g., spacer length), annealing program adjustment (e.g., temperature and ionic strength), and chemical supplements (e.g., betaine) (Supplementary Fig 15). With a better and more comprehensive understanding of the segment-segment complementation process in a complex system, optimisations of many kinds can then be applied in conjunction to push the complexity and controllability of DNA self-assembly to a new level.

Methods

Design, simulation and visualisation

The mesh models were designed using the AutoDesk Maya 2018 and Blender 3.2 computer graphics software suites^{27,28}. The scaffold-free routing scheme was implemented as a custom Python script in Maya (see Supplementary Software). Blender-designed meshes were exported as OBJ files and imported to Maya for running the script. The script uses the vHelix extension to Maya¹² to create and align helices along the edges of the mesh faces and connect their ends, thus generating a set of circular strands that wind around the boundaries of the faces and any possible holes. Steric zones that limit the helices' proximity at vertices were estimated from the average angle between edges at each vertex. For each edge, the maximum integral number of helical turns that does not extend the duplex into a steric zone was then selected as the helix length for that edge. The script nicks each helix at one or more loci of its constituent strands according to the standardised edge segmentation scheme presented in Supplementary Fig 1.

The same Maya Python script was used to export XML files containing the strand nucleotide pairing information. Applying the script parameter options, fixed-length poly-T spacers were inserted between connected helical segments at each mesh vertex to relax tension at the crossovers (2T in the case of the multilayer structures presented in Figs. 4, 3T for all the other structures). The exported XML files were then imported to the *Uniquimer* sequence design tool²⁹ to generate the DNA sequences. Sequences were generated using the following exclusion rules: (i) repeating base segments longer than a certain threshold (seven or eight bases) are not allowed, and (ii) four consecutive appearances of the same base are not allowed.

The nucleotide-level model visualisations in Figs. 2–4 were produced using the *oxView* design and visualisation tool³⁰, and the molecular dynamics simulations presented in Supplementary Movies 1–6 using the *oxDNA* simulation engine³¹, with visualisations by *oxView*.

Materials

DNA oligonucleotides (standard desalted) were purchased from GCATbio Co. Ltd (LS-PS-00005, for 1×1×1 cube, 11×6, 17×9, and 23×12 rectangle shapes, and Proteus) and from Integrated DNA Technologies (for Luck, Double Happiness, Flask, Cube and L-shape). DNA sequences can be found in Supplementary Data.

Structure formation, purification and yield quantification

To assemble the desired structures, component strands were mixed to an approximately equal molar final concentration of 100 nM and

Table 1 | Characteristics of some DNA wireframe nanostructure design methods

Method	BRAIDS	vHelix ^{12,24}	Daedalus/Athena ^{13,14}
Maximum size of structures	No intrinsic upper bound	ca. 14500 nt using M13 scaffold	ca. 14500 nt using M13 scaffold
Mesh complexity	Orientable 3D and 2D polygonal meshes with boundary	Sphere-equivalent 3D polygonal meshes ¹² , 2D orientable polygonal meshes with boundary ²⁴	Orientable 3D polygonal meshes ¹³ and 2D orientable polygonal meshes with boundary ¹⁴
Design algorithm runtime	Linear	Worst-case exponential	Linear
Edge element	Single duplex	Single duplex	Double duplex ¹³ , six-helix bundle ¹⁴
Strand routing principle	Oriented face cycles	A-trail	Spanning trees

annealed in 0.5 × TE buffer (5 mM Tris, pH 7.9, 1 mM EDTA) supplemented with varying concentrations of MgCl₂. Two annealing protocols, ‘ramp’ and ‘isothermal’, were employed to form the structures. For ramp annealing, the first ramp (from 90 °C to 61 °C) was conducted at a constant rate of 5 min per °C, followed by a second ramp (from 60 °C to 25 °C) at a constant rate of 120 min per °C. For isothermal annealing, the strands mixture was first denatured at 90 °C for 5 min, then annealed at a specific temperature between 40 °C to 50 °C for 72 h. Optimisation of annealing protocols, strand concentrations, and buffer conditions was performed on selected DNA structures and evaluated using native agarose gel electrophoresis (Supplementary Fig 15).

To purify the desired structures, annealed samples were subjected to 1% or 2% native agarose gel electrophoresis in an ice-water bath. The gels were prepared in 0.5 × TBE buffer (44.5 mM Tris, 44.5 mM boric acid, and 1 mM EDTA) supplemented with 10 mM MgCl₂ and pre-stained with SYBR Safe (Thermo Fisher Scientific). Target bands were excised and finely crushed in a Freeze’N Squeeze column (Bio-Rad), followed by centrifugation at 438 *g* for 3 min at 4 °C. The samples obtained from the column were collected for further analysis by AFM or cryo-EM.

To quantify the assembly yield, the intensity of the target band was compared to that of a standard band, such as the 5,000-base-pair band from a 1 kb DNA ladder mixture. The mass of the target band was determined using the intensity–mass correlation established with the standard band. The assembly yield was then calculated by dividing the mass of the target band by the total mass of all the input strands.

AFM imaging

The morphology of the 2D wireframe structures was characterised by AFM (Multimode 8, Bruker) in liquid ScanAsyst mode, using the C-type triangular tip from the SNL-10 silicon nitride cantilever chip (Bruker). A 40 µL drop of 0.5×TE buffer containing 10 mM MgCl₂ was applied to a freshly cleaved mica surface, followed by the addition of a 5 µL droplet of purified sample (2–10 nM) and an incubation of approximately 2 minutes. To enhance DNA–mica binding, an additional 10 µL of 10 mM NiCl₂ was added.

Cryo-EM imaging

Freshly purified samples were applied onto lacey carbon grids (Ted Pella) pre-treated with 0.1M MgCl₂. The grids were blotted for approximately 4–7 s and then rapidly frozen in liquid ethane using a Cryo Plunger 3 (Gatan). Micrographs of the samples were collected using an FEI Talos Arctica microscope operating at 200 kV, equipped with a K2 camera (Gatan) in movie mode.

Data availability

All the relevant data are contained in this article and its Supplementary Information materials, and are available from the corresponding author(s) upon request.

Code availability

The version of the BRAIDS software used to design the DNA meshes is available freely under the MIT open source license through Zenodo (<https://doi.org/10.5281/zenodo.15042492>) and the Supplementary Software zip file³².

References

- Seeman, N. C. & Sleiman, H. F. DNA nanotechnology. *Nat. Rev. Mater.* **3**, 17068 (2017).
- Seeman, N. C. Nucleic acid junctions and lattices. *J. Theor. Biol.* **99**, 237–247 (1982).
- Chen, J. H., Kallenbach, N. R. & Seeman, N. C. A specific quadrilateral synthesized from DNA branched junctions. *J. Am. Chem. Soc.* **111**, 6402–6407 (1989).
- Chen, J. & Seeman, N. C. Synthesis from DNA of a molecule with the connectivity of a cube. *Nature* **350**, 631–633 (1991).
- Winfrey, E., Liu, F., Wenzler, L. A. & Seeman, N. C. Design and self-assembly of two-dimensional DNA crystals. *Nature* **394**, 539–544 (1998).
- Goodman, R. P., Berry, R. M. & Turberfield, A. J. The single-step synthesis of a DNA tetrahedron. *Chem. Commun.* **40**, 1372–1373 (2004).
- Rothmund, P. W. K. Folding DNA to create nanoscale shapes and patterns. *Nature* **440**, 297–302 (2006).
- Douglas, S. M. et al. Self-assembly of DNA into nanoscale three-dimensional shapes. *Nature* **459**, 414–418 (2009).
- Dietz, H., Douglas, S. M. & Shih, W. M. Folding DNA into twisted and curved nanoscale shapes. *Science* **325**, 725 (2009).
- Han, D. et al. DNA origami with complex curvatures in three-dimensional space. *Science* **332**, 342 (2011).
- Douglas, S. M. et al. Rapid prototyping of 3D DNA-origami shapes with caDNAno. *Nucleic Acids Res.* **37**, 5001–5006 (2009).
- Benson, E. et al. DNA rendering of polyhedral meshes at the nanoscale. *Nature* **523**, 441–444 (2015).
- Veneziano, R. et al. Designer nanoscale DNA assemblies programmed from the top down. *Science* **352**, 1534–1534 (2016).
- Jun, H. et al. Rapid prototyping of arbitrary 2D and 3D wireframe DNA origami. *Nucleic Acids Res.* **49**, 10265–10274 (2021).
- Wei, B., Dai, M. & Yin, P. Complex shapes self-assembled from single-stranded DNA tiles. *Nature* **485**, 623–626 (2012).
- Ke, Y., Ong, L. L., Shih, W. M. & Yin, P. Three-dimensional structures self-assembled from DNA bricks. *Science* **338**, 1177 (2012).
- Ong, L. L. et al. Programmable self-assembly of three-dimensional nanostructures from 10,000 unique components. *Nature* **552**, 72–77 (2017).
- Wang, W. et al. Reconfigurable two-dimensional DNA lattices: static and dynamic angle control. *Angew. Chem. Int. Ed.* **60**, 25781–25786 (2021).
- Roth, B. Rigid and flexible frameworks. *Am. Math. Monthly* **88**, 6–21 (1981).
- Wang, W. et al. Complex wireframe DNA nanostructures from simple building blocks. *Nat. Commun.* **10**, 1067 (2019).
- Ellis-Monaghan, J. A. et al. Design tools for reporter strands and DNA origami scaffold strands. *Theor. Comput. Sci.* **671**, 69–78 (2017).
- Mohammed, A. & Hajj, M. Unknotted strand routings of triangulated meshes. In *Proceedings, 23rd International Conference on DNA Computing and Molecular Programming* 46–63 (Springer International Publishing, 2017). https://doi.org/10.1007/978-3-319-66799-7_4.
- Mohammed, A., Jonoska, N. & Saito, M. The topology of scaffold routings on non-spherical mesh wireframes. In *Proceedings, 26th International Conference on DNA Computing and Molecular Programming* 1–17 (Schloss Dagstuhl - Leibniz-Zentrum für Informatik, 2020). <https://doi.org/10.4230/LIPIcs.DNA.2020.1>.
- Benson, E. et al. Computer-aided production of scaffolded DNA nanostructures from flat sheet meshes. *Angew. Chem. Int. Ed.* **55**, 8869–8872 (2016).
- Truong-Quoc, C., Lee, J. Y., Kim, K. S. & Kim, D.-N. Prediction of DNA origami shape using graph neural network. *Nat. Mater.* **23**, 984–992 (2024).
- Sun, Z., Shen, Y., Wang, W. & Wei, B. DNA self-assembly optimization by betaine and its analogs. *Small* **24**, 2400930 (2024).
- Blender: The free and open source 3D creation suite. Blender Foundation, <https://www.blender.org/>.
- Maya: 3D animation and visual effects software. Autodesk, Inc., <https://www.autodesk.com/products/maya>.
- Wei, B., Wang, Z. & Mi, Y. Uniquimer: software of de novo DNA sequence generation for DNA self-assembly—an introduction and

- the related applications in DNA self-assembly. *J. Computational Theor. Nanosci.* **4**, 133–141 (2007).
30. Poppleton, E. et al. Design, optimization and analysis of large DNA and RNA nanostructures through interactive visualization, editing and molecular simulation. *Nucleic Acids Res.* **48**, e72–e72 (2020).
 31. Šulc, P. et al. Sequence-dependent thermodynamics of a coarse-grained DNA model. *J. Chem. Phys.* **137**, 135101 (2012).
 32. Wang, W. et al. Automated design of scaffold-free DNA wireframe nanostructures (this paper). ‘braids’, <https://doi.org/10.5281/zenodo.15042492> (2025).

Acknowledgements

We thank the Tsinghua University Branch of the China National Center for Protein Sciences (Beijing) for providing the facility support. We thank Dr. Jianlin Lei, Xiaomin Li, and Fan Yang for their assistance in cryo-EM data collection. This work is supported by National Key R&D Program of China (grant: 2021YFF1200200), Tsinghua University Spring Breeze Fund, grants from Tsinghua University Initiative Scientific Research Program (to B.W.), National Key R&D Program of China (grants: 2023YFC2306300 and 2021YFA1300204), the National Natural Science Foundation of China (grants: 31925023, 21827810, 31861143027), the Beijing Frontier Research Center for Biological Structure, the SXMU-Tsinghua Collaborative Innovation Center for Frontier Medicine and the Tsinghua-Peking Center for Life Sciences (to Y.X.), National Natural Science Foundation of China (grant: 32201175), Jiangsu Provincial Department of Science and Technology (No. BM2023009) (to W.W.), Academy of Finland (grant 311639, Algorithmic designs for biomolecular nanostructures) (to A.M.) and Finnish Cultural Foundation grant (Algorithmic design methods and tools for DNA nanotechnology) (to P.O.).

Author contributions

W.W. designed the experimental systems, performed the experiments, and wrote the paper, A.M. developed the software, designed several mesh models and rendered the corresponding DNA nanostructures, and wrote the paper, R.C. performed sample preparation for several DNA nanostructures, A.E. designed several mesh models and rendered the corresponding DNA nanostructures; S.C. performed cryo-EM imaging experiments; M.T. performed sample preparation for several DNA nanostructures; J.Y. performed cryo-EM imaging experiments; Y.X. supervised the sample characterization with cryo-EM; P.O. supervised the software development and wrote the paper; B.W. conceived and

supervised the project, and wrote the paper. All authors analysed the data and edited the paper.

Competing interests

The authors declare no competing interests.

Additional information

Supplementary information The online version contains supplementary material available at <https://doi.org/10.1038/s41467-025-59844-6>.

Correspondence and requests for materials should be addressed to Ye Xiang, Pekka Orponen or Bryan Wei.

Peer review information *Nature Communications* thanks Hyungmin Jun and the other, anonymous, reviewer(s) for their contribution to the peer review of this work. A peer review file is available.

Reprints and permissions information is available at <http://www.nature.com/reprints>

Publisher’s note Springer Nature remains neutral with regard to jurisdictional claims in published maps and institutional affiliations.

Open Access This article is licensed under a Creative Commons Attribution-NonCommercial-NoDerivatives 4.0 International License, which permits any non-commercial use, sharing, distribution and reproduction in any medium or format, as long as you give appropriate credit to the original author(s) and the source, provide a link to the Creative Commons licence, and indicate if you modified the licensed material. You do not have permission under this licence to share adapted material derived from this article or parts of it. The images or other third party material in this article are included in the article’s Creative Commons licence, unless indicated otherwise in a credit line to the material. If material is not included in the article’s Creative Commons licence and your intended use is not permitted by statutory regulation or exceeds the permitted use, you will need to obtain permission directly from the copyright holder. To view a copy of this licence, visit <http://creativecommons.org/licenses/by-nc-nd/4.0/>.

© The Author(s) 2025